ULTRA-LONG-PERIOD OSCILLATIONS IN EUV FILAMENTS NEAR TO ERUPTION: TWO-WAVELENGTH CORRELATION AND SEISMOLOGY

C. Foullon, E. Verwichte, and V. M. Nakariakov
Centre for Fusion, Space and Astrophysics, Department of Physics, University of Warwick, Coventry CV4 7AL, UK; claire.foullon@warwick.ac.uk

ABSTRACT

We investigate whether or not ultra-long-period oscillations in EUV filaments can be related to their eruption. We report new observations of long-period (∼10–30 hr) oscillatory motions in an apparently quiescent filament, as it crosses the solar disk in a 12 minute cadence *SOHO*/Extreme-Ultraviolet Imaging Telescope (EIT) 195 Å uninterrupted data set. This data set is chosen to explore characteristics of the filament oscillations depending on its eruptive behavior, which is observed while the filament is still on the disk. The periods are found to increase in a near-stable regime prior to eruption. For the two sequences reported so far, we compare and link the EUV filament oscillations with pulsations in full-disk solar EUV irradiance from *SOHO*/CELIAS/SEM 304 Å flux measurements. In intervals with stationary periods, we find that the 304 Å pulsations and the 195 Å filament oscillations have similar periodicities, but are phase-shifted by about a quarter of period. The two-wavelength correlation serves to show that, when the filament is the dominant dynamical feature but can no longer be tracked on the disk, the full-disk irradiance may provide a mean to identify the period increase prior to the filament eruption. We use the periods thus obtained to estimate the height increase of filaments' suspending coronal magnetic field lines, based on a magnetohydrodynamic (MHD) wave interpretation of the oscillations. The results are consistent with changes in prominence heights detected off-limb and thus support the seismological tool employed. Other interpretations connected with thermal overstability or MHD piston effect are possible. These theoretical predictions however do not explain the quarter-period shift between the two EUV-wavelength signals. In any case, the detected variations may provide a powerful diagnostic tool for the forecasting of prominence eruptions.

Key words: Sun: filaments – Sun: oscillations – Sun: prominences – Sun: transition region – Sun: UV radiation

Online-only material: color figures

1. INTRODUCTION

Solar prominences are cool and dense clouds of plasma in near equilibrium embedded in the corona. The strong association between eruptive prominences and coronal mass ejections (CMEs), which significantly affect the solar–terrestrial environment (e.g., Gopalswamy et al. 2003; Foullon et al. 2007), makes prominences important for understanding both the evolution of the global corona and space weather near Earth as well as in interplanetary space. Their investigation as a natural plasma laboratory is therefore a stepping stone in our understanding of the dynamics of the solar atmosphere, relevant for providing insight on the solar–terrestrial connections.

Solar prominences or filaments, seen on the limb or on the solar disk, are composed of small-scale ever-changing threads or fibrils. The channeling of plasma motions and of thermal conduction are controlled by the magnetic field, which also provides support to the prominence material against gravity (see Tandberg-Hanssen 1995, for a review). Quiescent prominences or filaments have been extensively studied in the Hα (H I) line from ground-based instruments, allowing uninterrupted observations for up to a few hours. They are rather dynamic structures displaying flows up to a few km s^{-1} and oscillations with a large range of periodicities. Until the detection of ultra-long-period oscillations (Foullon et al. 2004, hereafter F04), periodicities were customarily reported to range from less than 1 minute up to 90 minutes (e.g., Oliver & Ballester 2002).

Space-borne instruments allow us to study longer period variability of filaments. In F04, we revealed the presence of ultra-long-period oscillations (8–27 hr) in a coronal filament by using images taken from space at the wavelength of 195 Å by the Extreme-ultraviolet Imaging Telescope (EIT; Delaboudinière et al. 1995) on board *SOHO*, and following the filament for the first time over a long time range as it crossed the solar disk. The 195 Å (Fe xii) emission line is mostly sensitive to coronal plasmas at 1.6 MK. The observed intensity in this coronal bandpass is a line-of-sight integration of the absorbing filament and the emitting coronal material above it. The most pronounced oscillations with period around 12.1 hr were detected for nearly 6 days. Moreover, the 195 Å line-intensity variations were found to form a standing wave pattern, which covers 50–60 Mm along one end of the filament axis. We shall refer to this observation as Sequence 1.

This radically new result revised our knowledge of prominence oscillations (Ballester 2005; Banerjee et al. 2007). Subsequent observations of ultra-long periodicities (greater than 90 minutes) in filaments or prominences have been reported on seven separate days, albeit with shorter periods (less than 6 hr) and with no more than three cycles of oscillation (Isobe & Tripathi 2006; Pouget et al. 2006; Jing et al. 2006; Isobe et al. 2007; Pintér et al. 2008). However, they may be interpreted separately from the oscillations in Sequence 1, which was unique until now. In F04, we interpreted them either in terms of slow string magnetohydrodynamic (MHD) modes (e.g., Joarder & Roberts 1993) or as cyclic variations due to thermal overstability associated with peculiarities of the cooling/heating function and with the effect of neutrals (e.g., Bakhareva et al. 1992; Karpen et al. 2001; Müller et al. 2004). We note that, in all cases, the ultra-long periods are expected to increase with the increasing length of magnetic field lines supporting the filament, which may be related to a decreasing field strength. A third possible interpretation, which remains to be investigated, is in terms

of periodic motions of a density enhancement bouncing back and forth vertically under the effect of gravity in a stratified atmosphere, referred to as the "MHD piston effect" (Mackay & Galsgaard 2001). All these theoretical predictions do not explain the spatial structure of the oscillations along the filament, as shown in F04, but are useful to understand qualitatively the nature of the oscillations.

Yet, the detailed understanding of the plasma dynamics within, and around, prominences is a crucial step for answering many fundamental questions, which remain unanswered, such as

1. What is the configuration of their suspending coronal magnetic fields?
2. Are periodic changes in prominences always associated with their fibril structure?
3. What mechanisms are responsible for the heating mechanisms and stability of prominences?
4. What are the physical processes behind the eruption of filaments and what is the source of mass in the associated CMEs?

In Sequence 1, the filament was observed in 1999 (early September), during the rising phase of the solar activity, and erupted as a prominence over the West limb in the days after displaying the ultra-long-period pulsations. In the meantime, the ascent of the quiescent prominence, separate from the effect of rotation, was deduced by Foullon & Verwichte (2006) from comparing the results of an automated detection (combining image processing of four synoptic EIT images, taken at different wavelengths in the EUV) with a theoretically apparent height profile (in time or equivalent Carrington longitude) of the prominence rotating over the limb. The prominence height may be used as a criterion for eruption, as proposed by Filippov & Den (2001) in a study of off-limb Hα prominences and shown by Foullon & Verwichte (2006) for EUV prominences. This criterion may be related to prominence mass loading models (see Fong et al. 2002; Low et al. 2003, and references therein), which require information about the plasma distribution in the corona (e.g., prominence mass or coronal cavity). The total mass of a quiescent prominence is significant for understanding, at the time of its eruption, the rise (e.g., Švestka et al. 1995), the acceleration, and the source of mass of the associated CME. One important question we wish to answer is whether or not the observed cyclic behavior can be related to the eruption. Ultra-long-period pulsations are likely related to the thermodynamics and the global stability of prominences. If the slow rising phase of the filament is accompanied by a gradual ascension and expansion of the overlying arcade, then the ultra-long periods are expected to increase, provided the other parameters remain constant. Thus, a positive answer would make the detected variations a powerful diagnostic and forecasting tool for the prediction of prominence eruption.

In Section 2, we study a quiescent filament in a new EIT data set (2003 March–April) and detect ultra-long-period oscillations by performing a similar analysis as in F04. Unlike Sequence 1, this data set is chosen to explore characteristics of the filament oscillations depending on its eruptive behavior, which is observed while the filament is still on the disk. We shall refer to this sequence as Sequence 2. In Section 3, for both sequences thus analyzed, we compare and link the EUV filament oscillations at 195 Å with pulsations in full-disk solar EUV irradiance at 304 Å. The oscillation characteristics and the two-wavelength diagnostics thus obtained are used in Section 4

to discuss the implications of the detected variations for the forecasting of prominence eruptions and the possible theoretical interpretations of the ultra-long-period oscillations. Section 5 summarizes our conclusions.

2. IMAGE DATA ANALYSIS OF SEQUENCE 2

We consider a 12 minute cadence *SOHO*/EIT 195 Å uninterrupted data set covering 8 days from 2003 March 27 (Time = 0 hr). In this data set, a curved EUV filament, elongated in latitude, crosses the solar northern hemisphere (Figures 1(a) and (b)). The filament is detected to rise and to erupt while on the disk. The time of the eruption is on April 2 around 04 UT. The ascent of this midlatitude filament cannot be ascertained while the filament is in the middle of the disk. As it rotates closer to the West limb, the first distinct rise of the filament occurs around 21:00 UT on April 1 (Time = 141 hr), as observed with EIT 195 Å running difference images and Hα solar images. This is shown in the running difference 195 Å image of Figure 1(c), where the rising of the dark EUV filament against the brighter disk is detected in a dimming at its upper edge (as shown between white lines). The filament rise is also evident from comparison of Hα solar images from the Big Bear Solar Observatory (BBSO) in panels (a) and (d) of Figure 1. The rising material of the filament is then seen in absorption against the disk by EIT 304 Å at 1:20 UT on April 2 (Time = 145.3 hr, Figure 1(e)). The eruption is captured by EIT 195 Å from 0:11 UT on April 2 (Time = 144.1 hr), showing the formation of an arcade of loops moving upward and with footpoint separations expanding in the northern part of the filament, followed by a postflare linear structure underlying the filament channel (Figure 1(f)). Starting at 3:54 UT on April 2 in the outer corona, LASCO coronagraphs detect a faint streamer outflow in the NW and slight gusty outflows in the SW presumably associated with this eruption (see CME LASCO catalogue[1]).

Prior to its eruption, we detect ultra-long-period emission changes in the curved southern part of the EUV filament. Data are processed as in F04 and as summarized below. For a given EIT 195 Å full-disk solar image, the heliographic projection (i.e., orthographic projection of the solar disk) is deduced, as illustrated in Figures 2(a) and (b). In addition, the solar Carrington rotation is corrected, so that, in the data series obtained, any feature rotating with the Sun on the solar disk evolves at a nearly stationary position. In Figure 2(b), the overlaid square (S5-N85, $L = 170$–260) encloses the region where the EUV filament is observed, and for which a time sequence of projected and derotated images is produced. We consider a rectangular region of interest (ROI), where oscillations are observed. This is shown in the one particular sequence snapshot in Figure 2(c). Here, with maps of size 360×360 pixels, a spatial resolution of 2 pixels per degree (corresponding to 6.08 Mm per pixel) is achieved. The ROI is $10°.5$ long and $1°.5$ wide ($1° \sim 2$ pixels ~ 12.15 Mm).

The intensity is averaged over all points in the chosen region, thus giving a time series (a couple of images with "missing blocks" overlying the ROI are discarded). The series are resampled with the largely prevailing time cadence of 12 minutes (0.2 hr), yielding the regular time series I for the averaged intensity in the ROI. Oscillatory variations are visible in I, shown as a thin line in Figure 3(a). To examine first the oscillations between Times 50 and 100 hr, I is detrended with a 20 hr boxcar running average. The trend, denoted I_o and
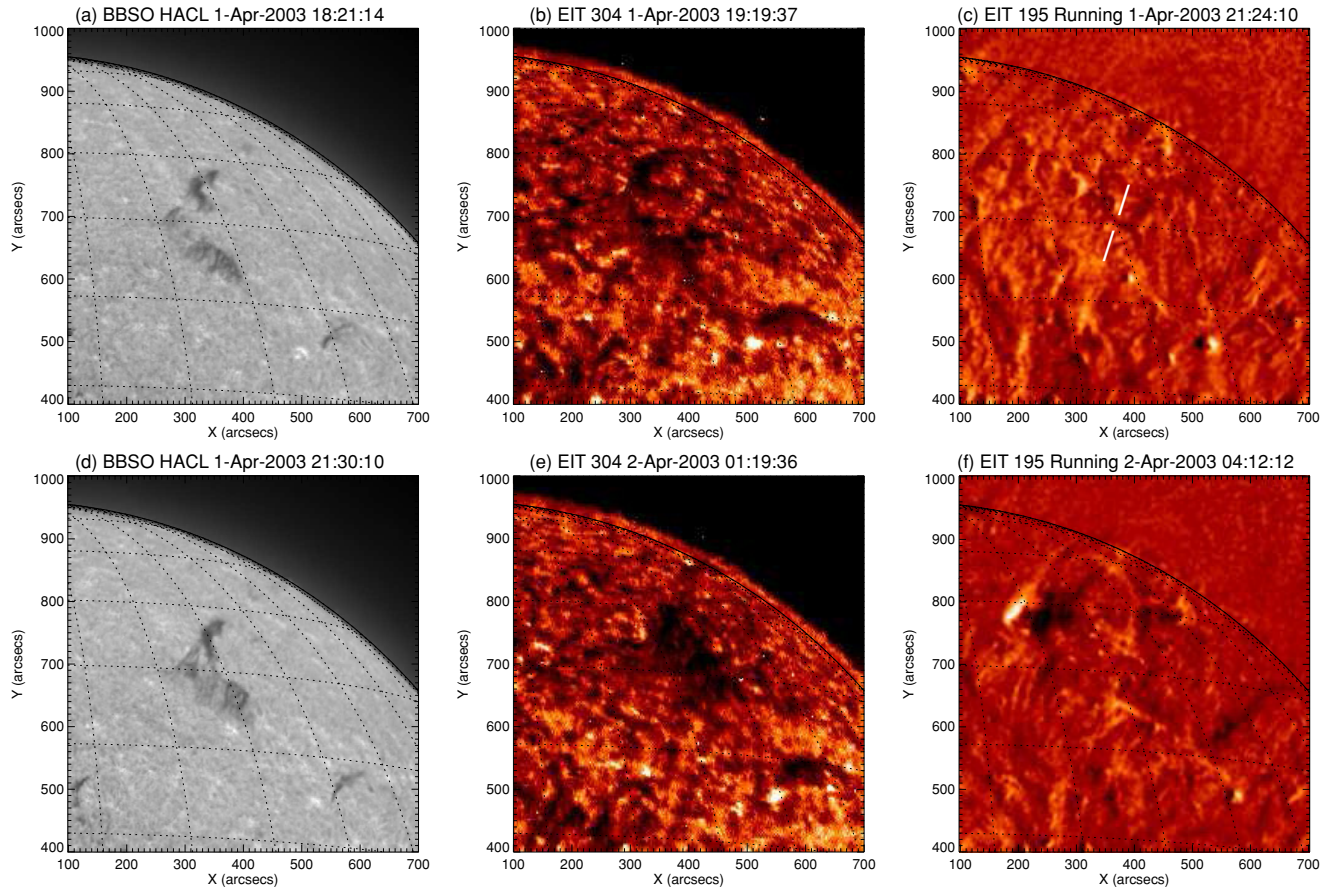

Figure 1. Snapshots of the solar NW sector in (left) Hα (©BBSO), (middle) EIT 304 Å, and (right) 195 Å running difference images, showing (a and b) quiescent, (c–e) rising, and (f) erupting phases of a curved filament on 2003 April 1–2 (from 18:21 UT on April 1 to 4:12 UT on April 2). In the running difference 195 Å image of panel (c), the rising of the dark EUV filament against the brighter disk is detected in a dimming at its upper edge, as shown between white lines.

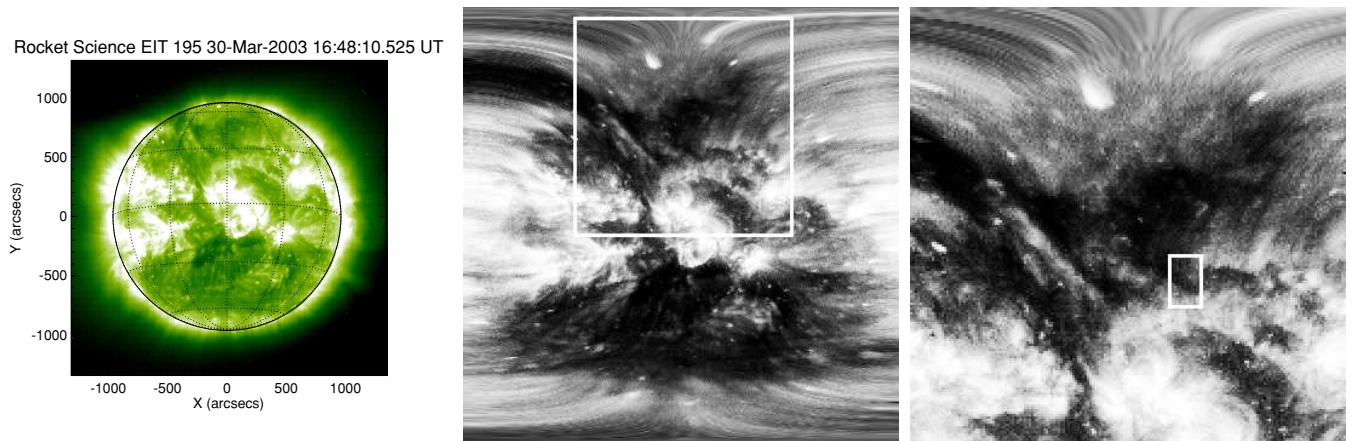(A color version of this figure is available in the online journal.)

Figure 2. (a) EIT 195 Å full-disk solar image taken on 2003 March 31, 16:48 UT. (b) The corresponding heliographic projection of the solar disk; the overlaid square (S5-N85, $L = 170$–260) shows a curved filament. (c) The corresponding snapshot; a rectangular ROI on the curving part (centered at N28, $L = 220$) is overlaid in white.

(A color version of this figure is available in the online journal.)

shown as a thick line in Figure 3(a), is mostly due to the "limb brightening." The limb brightening is caused by the bright loops from active regions and may hide away an EUV filament near the limbs. The relative intensity $I/I_o - 1$ is shown in Figure 3(b). The amplitude of the intensity variations reaches approximately 10% of the background intensity.

A Morlet wavelet power spectrum of this time series is shown in Figure 3(c). The 95% confidence level (including red noise) was computed according to Torrence & Compo (1998). Two distinct ranges of periodicities are detected at different epochs or phases. In the first part (Time = 50–100 hr), which spans 4–5 cycles of oscillation, the dominant periods are seen to increase
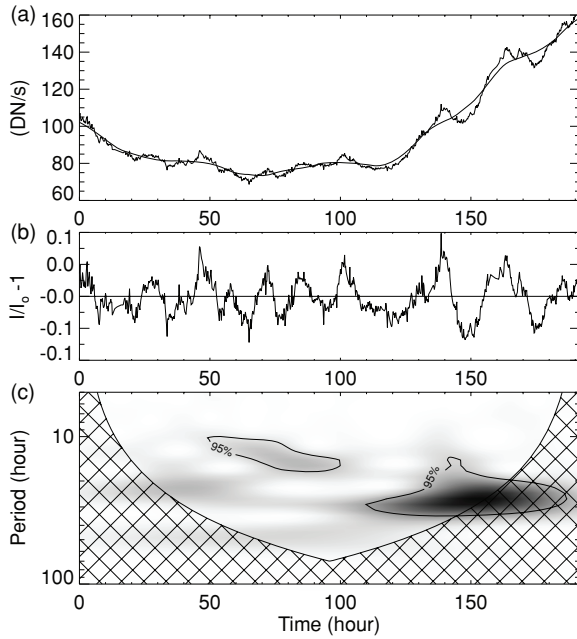
Figure 3. Ultra-long-period oscillations detected in an EIT 195 Å data set starting 2003 March 27. (a) Averaged intensity I in the ROI (thin line) and 20 hr boxcar running average I_o (thick line). (b) Intensity time series $I/I_o - 1$. (c) Corresponding Morlet wavelet power spectrum: increasing gray level is used to represent increasing power; significant power is within the 95% confidence level contour (including red noise) and outside the hatched cones of influence.

from about 10 to 20 hr. In the second part, spanning 3 cycles of oscillation, the dominant periods are detected around 30 hr. The transition between the two phases occurs around Time = 100–110 hr. Since this is about 40 hr before the first distinct rise of the filament is detected (on the disk as it approaches the West limb), this draws a link between the 30 hr periodicity and the global nature of the eruption, which itself includes more subtle time histories (e.g., Sterling & Moore 2004).

3. TWO-WAVELENGTH DIAGNOSTICS FOR SEQUENCES 1 AND 2

During days of the Sequences 1 and 2 reported by F04 and above, pulsations have been detected by Gangopadhyay et al. (2007) in the 260–340 Å (first-order channel 1) full-disk solar flux measurements, from the Charge, Element, and Isotope Analysis System/Solar EUV Monitor (CELIAS/SEM) onboard *SOHO* (Hovestadt et al. 1995). The first-order CELIAS/SEM 260–340 Å channels are dominated by the 304 Å emission line, where the most significant He II line is sensitive to plasma in the upper transition region at 0.08 MK and dominates on disk above the quiet Sun, and the Si XI line, sensitive to temperatures at 1.6 MK, is significant in active regions and dominates off-limb. The pulsations detected by SEM have similar periods to the ones detected in the 195 Å EUV filaments: around 12 and 30 hr for Sequences 1 and 2, respectively. In Sequence 2, the amplitudes of the 10–20 hr oscillations detected in the 195 Å ROI are not visible in the full-disk 304 Å irradiance. Although they are spatially unresolved full-disk flux measurements, CELIAS/SEM data are taken at the high cadence of 15 s, while the spatially resolved EIT 304 Å images, which are taken every 6 hr in the synoptic program, are not best suited to detect the shortest oscillations.

To determine whether the oscillatory phenomena detected in two different bandpasses, one with spatial resolution in the EUV filament and the other in full-disk solar EUV irradiance, are related, we compare characteristic periods, phases, and amplitudes of intensity variations $I/I_o - 1$ between the two data sets. This is presented for each sequence, first in Figure 4 for Sequence 2, starting 2003 March 27 reported here and then in Figure 5 for Sequence 1, starting on 1999 August 29 reported by F04. In both figures, the variation time series are shown where I is (a) the 12 minute cadence EIT 195 Å averaged intensity time series in the ROI and (b) the 5 minute average CELIAS/SEM 304 Å flux (technically the average of the two first-order CELIAS/SEM 260–340 Å channels). To study the dominant periodicities detected in both data sets, the trend I_o is a 50 hr boxcar running average in Sequence 2 and a 14 hr boxcar running average in Sequence 1. In Figure 4 (Sequence 2), the 10–20 hr oscillations (Time = 50–100 hr) are still visible in panel (a) despite the 50 hr boxcar detrending, but are not visible in panel (b).

Nevertheless, there are intervals in each sequence where the time series appear similar, with stationary periods. In particular, for a 4-day interval indicated between vertical dashed lines, respective power spectra are computed and shown in panels (c) and (d) below. As illustrated in Torrence & Compo (1998), the global wavelet spectrum is normalized (with the squared wavelet variance σ^2) and compared to the normalized Fourier power spectrum. The global wavelet spectrum gives a smoothed version of the power spectrum. A higher frequency resolution is achieved by computing the Lomb–Scargle periodogram of the non-sampled and detrended time series (Scargle 1982; Horne & Baliunas 1986). The 95% confidence level for the periodogram was computed according to Bai & Cliver (1990).

For Sequence 2, the highest peak in the spectra corresponds to a dominant period of 33.5 ± 6 hr in EIT 195 Å and a period of 38 ± 8 hr in SEM 304 Å. The dominant periods belong to the same bin between 28 and 40 hr in the Fourier spectra and fall in the band between 25 and 43 hr, where the power is above confidence level. For Sequence 1, all spectra peak at the period of 12 hr and lower peaks can be distinguished near 8 and 15 hr. Thus, for the two sequences reported, the ultra-long-period oscillations in EUV filaments can be linked with variations in solar EUV irradiance.

However, the EUV ROI and solar flux are taken at two separate wavelengths. For Sequence 2, the longer periods of 30 hr allow us the use of EIT 304 Å images taken at the time cadence of 6 hr to show the corresponding EIT 304 Å variation time series in the ROI (connected diamonds in Figure 4(a)). In the interval Time = 110–170 hr, we note a phase shift of about 5 hr between the 304 and 195 Å time series, the 195 Å following the 304 Å time series. To confirm and characterize the phase shifts between the time series at separate wavelengths, we perform the cross-correlation (Fuller 1995) between the ROI 195 Å intensity and full-disk 304 Å flux variation time series, as shown versus time lags in Figure 6. The coefficients for the narrowband signals centered on the dominant periods of each sequence reach statistically significant peaks (above 0.8 in all cases), indicating a good correlation and phase shifts of about 2 ± 1 and 4 ± 3 hr for the sequences with (Sequence 1) 12 hr and (Sequence 2) 30 hr periods, respectively (the 195 Å following the 304 Å time series). Although the highest cross-correlation coefficients in the original signals (dotted lines in Figure 6) are not statistically significant, they are reached for similar time lags. We conclude that, for the two sequences studied so far, the two EUV-wavelength ultra-long-period oscillations are phase-shifted by about a quarter of period.
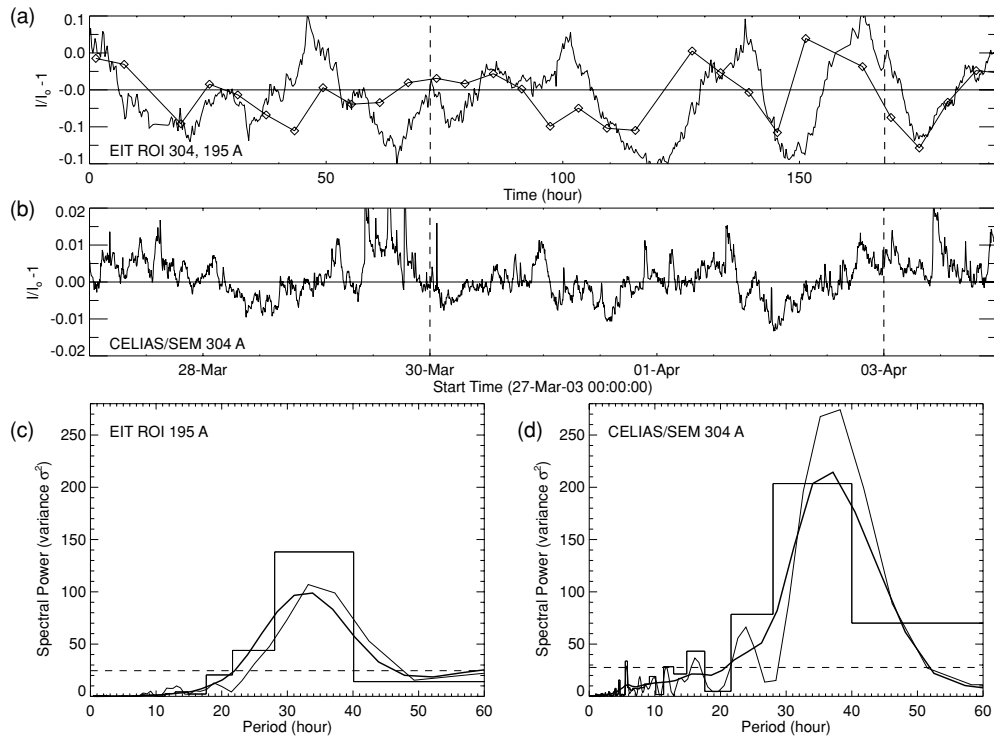
Figure 4. Comparison between intensity variations for Sequence 2, starting 2003 March 27. Panels (a) and (c) show, respectively, intensity variations and the corresponding power spectra for the averaged intensity in the EIT 195 Å ROI. Panels (b) and (d) show similar plots for the solar flux at 304 Å from CELIAS/SEM. The spectra are computed for a 4-day interval starting on 2003 March 30 (indicated between vertical dashed lines in panels (a) and (b)). (a) and (b) Intensity time series $I/I_o - 1$, where I_o is a 50 hr boxcar running average. In panel (a), the additional line with diamond symbols is for the averaged intensity in the EIT 304 Å ROI. (c) and (d) Lomb–Scargle periodogram (thin solid), normalized Fourier power spectrum (histogram mode) and normalized global wavelet spectrum (thick solid). The horizontal dashed line is the 95% confidence level for the periodogram.
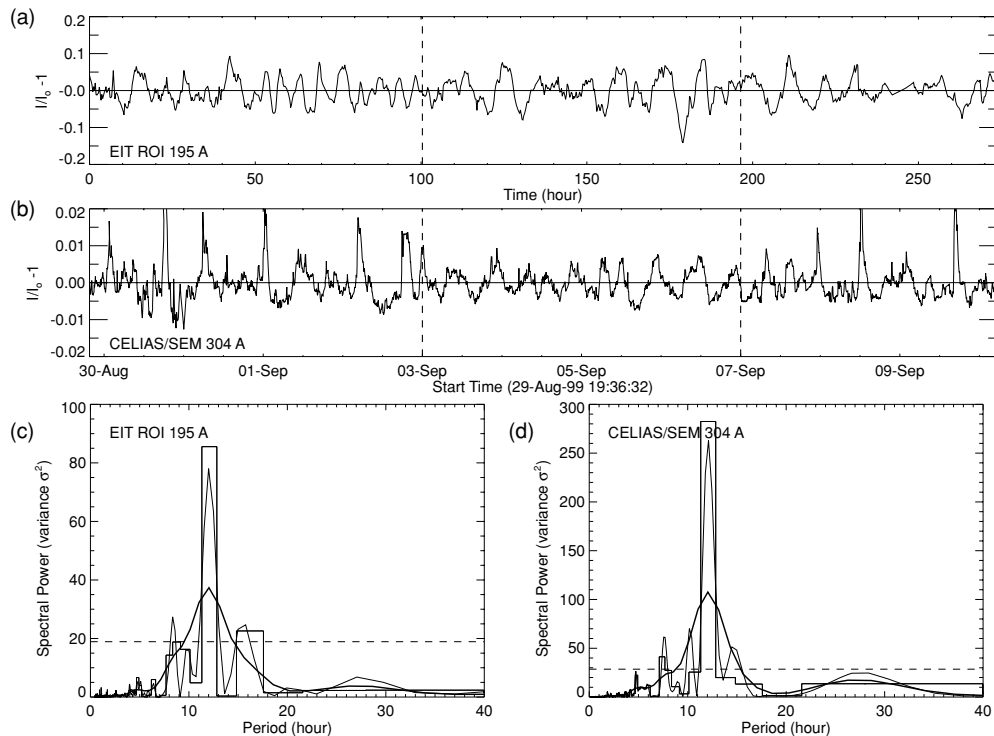

Figure 5. Comparison between intensity variations for Sequence 1, starting 1999 August 29 (19:36:32 UT). Panels (a) and (c) show, respectively, the intensity variations and the corresponding power spectra for the averaged intensity in the EIT 195 Å ROI. Panels (b) and (d) show similar plots for the solar flux at 304 Å from CELIAS/SEM. The spectra are computed for a 4-day interval starting on 1999 September 3 (indicated between vertical dashed lines in panels (a) and (b)). Details are the same as in Figure 4, but in panels (a) and (b) I_o is a 14 hr boxcar running average.
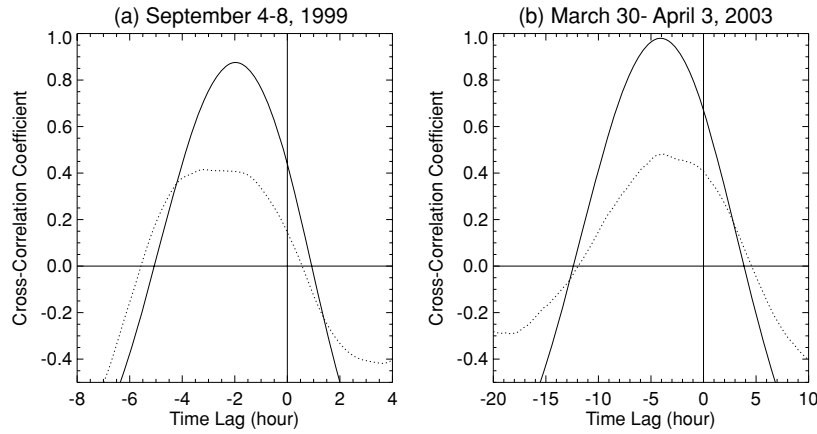
Figure 6. Cross-correlation coefficients vs. lag times between EIT 195 Å and CELIAS/SEM 304 Å variation time series in 4-day intervals (indicated between vertical dashed lines in panels (a) and (b) of Figures 4 and 5, respectively). The coefficients are shown for the original variation signals (dotted lines) and for the narrowband signals (plain lines) centered on periods of (a) 10–15 hr and (b) 25–43 hr.

Finally, the amplitudes of the intensity variations may be compared and interpreted in terms of the size of the EUV filament relative to the solar disk. Figure 4(a) shows that the relative amplitudes in the EUV filament are similar between 195 and 304 Å: the variation amplitudes are of the order of 10% of the background intensity ($|I/I_o - 1| = 0.1$). The 21×11 pixel ROI represents about 0.2% of the solar map (360×360 pixels) or of the solar disk (equivalent to $\pi 180^2$ pixels), so that if the variations are limited to the ROI but are the only variations to be detected in the full-disk intensity, then the full-disk intensity variation amplitude, $|F - F_o|$, may represent 0.2% of the ROI intensity variation amplitude, $|I - I_o|$. The full-disk 304 Å variation amplitude is of the order of 1% of the solar background flux ($|F/F_o - 1| = 0.01$). Therefore, for these variations to be directly related to the ROI variations, the average intensity of the full disk has to be 50 times the background intensity in the ROI ($I_o/F_o = 0.02$). This factor is reasonable given that the 304 Å intensity in the ROI is dominated by the lower intensity levels above the absorbing filament, while the 304 Å full-disk intensity is dominated by higher intensity levels from the contributing active regions, on-disk and off-limb, and the transition region above the quiet Sun.

4. DISCUSSION

4.1. Pre-eruption Period Increase

In Section 2, we presented new observations of ultra-long-period oscillations in an EUV filament, showing that the sequence reported by F04 is not an isolated sequence. In this new sequence, though, we find that the periods of the oscillations increase (from 10 to 30 hr) prior to the filament eruption. According to the MHD wave and non-thermal equilibrium interpretations, this period increase indicates a slow rise of the suspending magnetic field lines in a near-stable regime prior to the filament eruption. This should result in the accompanying slow rise of the filament, which has been reported days prior to its eruption in other events (e.g., Foullon & Verwichte 2006; Zhou et al. 2006).

The link with the solar EUV irradiance as demonstrated in Section 3 may provide an additional mean to detect these period changes, in particular while the filament rotates over the limb. However, in Sequence 2, the amplitudes of the 10–20 hr period oscillations do not dominate in the full-disk 304 Å irradiance. In spite of this, we test if the solar irradiance in Sequence 1 shows period increase prior to the eruption. In
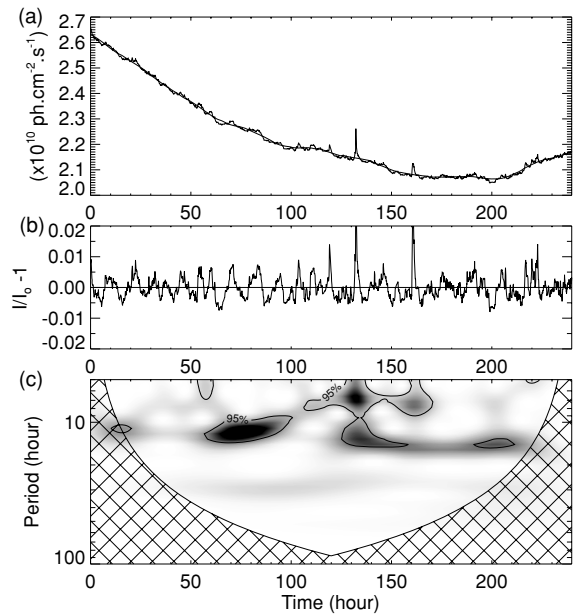

Figure 7. Ultra-long-period oscillations detected in CELIAS/SEM 304 Å data set starting 1999 September 3. (a) 5 minute averaged flux I (thin line) and 14 hr boxcar running average I_o (thick line). (b) Intensity time series $I/I_o - 1$. (c) Corresponding Morlet wavelet power spectrum: increasing gray level is used to represent increasing power; significant power is within the 95% confidence level contour (including red noise) and outside the hatched cones of influence.

Figure 7, variations in full-disk 304 Å irradiance are shown for the time interval 1999 September 3–13. The first part is an interval with 12 hr periodicities detected in the filament ROI (Figure 5) and the latter part includes the pre-eruption phase, when the filament can no longer be tracked on the disk. Despite a couple of brightenings in the solar flux, the wavelet power spectrum reveals an overall period increase from 12 to 15 hr. The combined data sets and their analysis summarized in Table 1 show that the full-disk observations may provide means to identify the period increase prior to the filament eruption, provided that the filament is the dominant dynamical feature on the disk.

The period increase observations validate both the MHD wave and non-thermal equilibrium models. The implications for the length and height of a semicircular coronal arcade and therefore the strength of the suspending field are qualitatively equivalent (F04). In particular, the slow string MHD mode (e.g., Joarder &

Table 1
Summary of Oscillatory Characteristics for the Two Observational Sequences Discussed

		Sequence 1	Sequence 2
ROI EIT 195 Å data set			
Start date		1999 Aug 29 19:36:32 UT	2003 Mar 27 00:00:00 UT
End date		1999 Sep 10 05:24:16 UT	2003 Apr 4 00:00:00 UT
Events included?	(a) Period increase	No, outside of this data set	Yes, in this data set
	(b) Eruption	No, outside of this data set	Yes, in this data set
Subinterval for two-wavelength analysis		1999 Sep 3/1999 Sep 7	2003 Mar 30/2003 Apr 3
	Duration (hr)	96	96
	Running length (hr)	14	50
	Dominant period (hr)	12	28–40
	Phase shift 195–304 Å (hr)	2 ± 1	4 ± 3
Significant events			
(a) Period increase: Data set		Solar SEM 304 Å	ROI EIT 195 Å
	Interval dates	$\sim$ 1999 Sep 5/1999 Sep 12	$\sim$ 2003 Mar 29/2003 Mar 31
	Duration (hr)	$\sim$150	$\sim$ 50
	Running length (hr)	14	20
	Period start–end (hr)	12–15	10–20
	Number of cycles	$\sim$ 10–12	$\sim$ 4–5
(b) Eruption time		1999 Sep 14 (5–8 UT)	2003 Apr 2 (01:20-4 UT)

Notes. For each sequence, the table shows the EIT 195 Å data set used to track the ROI on the disk, the significant events included in this data set, i.e., (a) period increase and (b) eruption, the subintervals used and results for the two-wavelength analysis (Section 3). Details of the significant events are (a) the data sets used and results for the period increase analysis and (b) the eruption time.

Roberts 1993) interpretation predicts a period ratio proportional to the square root of the loop length ratio. Therefore, the rise of the filament is expected to follow this rule, viz.,

$$\frac{P_2}{P_1} = \sqrt{\frac{r_2}{r_1}}, \qquad (1)$$

where indices 1 and 2 indicate two filament stages, characterized with period of oscillation, P, and radius or height of the semicircular arcade, r.

As shown by Foullon & Verwichte (2006), the filament in Sequence 1 rose by $\Delta r \geqslant 0.02\ R_\odot \sim 14$ Mm, between September 6 at 6:36 UT and September 11 at 12 UT (from the apparent detection on the West limb of prominence material at the location of a coronal hole on the disk). In the meantime, the oscillation periods increased from 12 to 15 hr. Therefore, the initial height of the filament suspending field on September 6, r_1, is given by Equation (1) with $r_2 = r_1 + \delta r$, $P_1 = 12$ and $P_2 = 15$ h, that is $r_1(= \Delta r / ((P_2/P_1)^2 - 1)) \geqslant 0.035\ R_\odot = 24$ Mm, and the coronal arcade reaches $r_2 \geqslant 0.055\ R_\odot \sim 38$ Mm on September 11. These heights are consistent with the longitudinal profiles of the EUV prominences on the East and West limbs shown in Figure 10 of Foullon & Verwichte (2006). Thus, these results validate the seismological tool employed.

In Sequence 2, the period increase phase (Time = 50–100 hr) occurs while the midlatitude filament is on the disk, without any information about the filament rise. From Equation (1) with $P_1 = 10$ and $P_2 = 20$ hr, we deduce that the suspending field may have risen by an amount that is ($\delta r / r_1 = (P_2/P_1)^2 - 1 =$) three times the initial height. Thus, the two sequences show that the suspending field may rise significantly and presumably locally at an endpoint or local curve of the filament channel. Such local ascent may serve to kink the field lines of the filament suspending arcade, increasing the pinch or helicity content and thus the probability of eruption (e.g., Ashbourn & Woods 2002).

4.2. Mechanisms for the Ultra-Long-Period Oscillations

During the pulsation intervals from Sequences 1 and 2, no similar power peak was found in the GOES soft and hard X-ray

flux (Gangopadhyay et al. 2007). We think possible to link this lack of correlation between the coronal EUV emission (namely, from the EIT 195 Å channel) and the soft X-ray emission to a specific brightness difference in polar regions detected with spatially resolved solar images. As revealed in aggregates of Carrington maps of the Sun, the polar regions (presumably loop footpoints) are brighter in coronal EUV emission than in soft X-ray (Benevolenskaya et al. 2002, Figure 1, mark II) and are connected via giant loops (visible as diffuse structures in soft X-ray) to the following parts of active regions at midlatitude. In between are filaments located at the magnetic neutral lines, with typical "coronal cavities" surrounding them (Benevolenskaya et al. 2001). The high-latitude structures or giant loops appear mostly during the rising phase of the solar cycle and migrate poleward until the next cycle.

We believe an important feature that may help to discriminate between theoretical predictions is the quarter-period shift between the two signals, obtained at separate wavelengths and both in the EUV. In the slow mode MHD wave scenario, it may be helpful to consider the Prominence-Corona Transition Region (PCTR) slow modes (Soler et al. 2007), which are predicted to produce large displacements of the plasma along the magnetic field inside the transition region. The detected 304 Å oscillations with typical upper transition region temperatures could be interpreted in terms of such modes. It is much less clear how to interpret the 195 Å intensity fluctuations. They may be caused by either the area of the PCTR/prominence plasma occulting the source plasma or the PCTR/prominence transparency/opacity/density that is periodically changing.

Other interpretations are connected with thermal overstability (e.g., Kuin & Martens 1982) or MHD piston effect (Mackay & Galsgaard 2001). As suggested in F04, such periodic dynamical events might also trigger the resonance with modes of the filament. Depending on the simulation parameters, the thermal non-equilibrium model by Karpen et al. (2006) is able to yield primary condensation periods (formation to formation) ranging from 9.5 hr to several days, and often showing 2 hr period subcycles of unsteady flow superposed on each condensation life cycle. These subcycles could complicate the

detection of primary condensation periods and any phase shift of that order. The model by Karpen et al. (2006) also predicts comparable speeds for prominence plasma at both chromospheric and transition-region temperatures, implying in-phase motions between the two plasmas. The quarter-period shift between the two EUV-wavelength time series may bring additional elements for such models to consider. However, better spatial and temporal resolutions than used here would be desirable.

5. CONCLUSION

New observations of long-period (~ 10–30 hr) oscillatory motions in an apparently quiescent EUV filament are presented, showing an increase of the oscillation periods prior to the filament eruption. For the two sequences reported so far and in intervals with stationary periods, the 195 Å EUV filament oscillations and pulsations in full-disk 304 Å flux measurements are correlated, with similar periodicities, but phase-shifted by about a quarter of period (see Table 1). The two-wavelength correlation serves to show that, when the filament is the dominant dynamical feature but can no longer be tracked on the disk, the full-disk irradiance may provide a mean to identify the period increase prior to the filament eruption. We conclude that ultra-long-period oscillations in EUV filaments can be related to their eruption, with their slow increasing periods over several days indicating presumably a rise of the filament and suspending magnetic arcade in a near-stable regime. The periods can then be used to estimate the height increase of filaments' suspending coronal magnetic field lines, based on an MHD wave interpretation of the oscillations. The results are consistent with changes in prominence heights detected off-limb and thus validate the seismological tool employed. Other interpretations connected with thermal overstability or MHD piston effect are possible. These theoretical predictions however do not explain the quarter-period shift between the two EUV-wavelength signals.

In either case, (1) when the filament is the dominant dynamical feature but can no longer be tracked on the disk or (2) when the filament is on the disk, the detected variations may provide a powerful diagnostic tool for the forecasting of prominence eruptions. Indeed, the local ascent of the filament, suggested by the local detection of the ultra-long-period oscillations and their period increase, can be linked with an increased probability of eruption. However, spatially resolved images from the twin Solar–Terrestrial Relations Observatory (STEREO) spacecraft or the Solar Dynamics Observatory (SDO) are needed to investigate further these phenomena. Although operating in an extended solar minimum, the spatially resolved SECCHI/EUVI images from the STEREO mission may be able to overcome both the cases of multiple dynamical events and the off-limb issue. Much improved time cadence and spatial resolution from EUVI and from instruments onboard the future SDO mission will provide means to compare multiwavelength images of EUV filaments in greater details.

REFERENCES

Ashbourn, J. M. A., & Woods, L. C. 2002, ApJ, 568, 1049
Bai, T., & Cliver, E. W. 1990, ApJ, 363, 299
Bakhareva, N. M., Zaitsev, V. V., & Khodachenko, M. L. 1992, Sol. Phys., 139, 299
Ballester, J. L. 2005, Space Sci. Rev., 121, 105
Banerjee, D., Erdélyi, R., Oliver, R., & O'Shea, E. 2007, Sol. Phys., 246, 3
Benevolenskaya, E. E., Kosovichev, A. G., Lemen, J. R., Scherrer, P. H., & Slater, G. L. 2002, ApJ, 571, L181
Benevolenskaya, E. E., Kosovichev, A. G., & Scherrer, P. H. 2001, ApJ, 554, L107
Delaboudinière, J.-P., et al. 1995, Sol. Phys., 162, 291
Filippov, B. P., & Den, O. G. 2001, J. Geophys. Res., 106, 25177
Fong, B., Low, B. C., & Fan, Y. 2002, ApJ, 571, 987
Foullon, C., & Verwichte, E. 2006, Sol. Phys., 234, 135
Foullon, C., Verwichte, E., & Nakariakov, V. M. 2004, A&A, 427, L5
Foullon, C., et al. 2007, Sol. Phys., 244, 139
Fuller, W. A. 1995, Introduction to Statistical Time Series (New York: Wiley)
Gangopadhyay, P., Didkovsky, L., Ghadimi, H., Wieman, S., & Judge, D. L. 2007, ApJ, 670, 1414
Gopalswamy, N., Shimojo, M., Lu, W., Yashiro, S., Shibasaki, K., & Howard, R. A. 2003, ApJ, 586, 562
Horne, J. H., & Baliunas, S. L. 1986, ApJ, 302, 757
Hovestadt, D., et al. 1995, Sol. Phys., 162, 441
Isobe, H., & Tripathi, D. 2006, A&A, 449, L17
Isobe, H., Tripathi, D., Asai, A., & Jain, R. 2007, Sol. Phys., 246, 89
Jing, J., Lee, J., Spirock, T. J., & Wang, H. 2006, Sol. Phys., 236, 97
Joarder, P. S., & Roberts, B. 1993, A&A, 277, 225
Karpen, J. T., Antiochos, S. K., Hohensee, M., Klimchuk, J. A., & MacNeice, P. J. 2001, ApJ, 553, L85
Karpen, J. T., Antiochos, S. K., & Klimchuk, J. A. 2006, ApJ, 637, 531
Kuin, N. P. M., & Martens, P. C. H. 1982, A&A, 108, L1
Low, B. C., Fong, B., & Fan, Y. 2003, ApJ, 594, 1060
Mackay, D. H., & Galsgaard, K. 2001, Sol. Phys., 198, 289
Müller, D. A. N., Peter, H., & Hansteen, V. H. 2004, A&A, 424, 289
Oliver, R., & Ballester, J. L. 2002, Sol. Phys., 206, 45
Pintér, B., Jain, R., Tripathi, D., & Isobe, H. 2008, ApJ, 680, 1560
Pouget, G., Bocchialini, K., & Solomon, J. 2006, A&A, 450, 1189
Scargle, J. D. 1982, ApJ, 263, 835
Soler, R., Oliver, R., & Ballester, J. L. 2007, Sol. Phys., 246, 73
Sterling, A. C., & Moore, R. L. 2004, ApJ, 602, 1024
Švestka, Z., Fárník, F., Hudson, H. S., Uchida, Y., Hick, P., & Lemen, J. R. 1995, Sol. Phys., 161, 331
Tandberg-Hanssen, E. 1995, The Nature of Solar Prominences (Dordrecht: Kluwer)
Torrence, C., & Compo, G. P. 1998, Bull. Am. Meteorol. Soc., 79, 61
Zhou, G. P., Wang, J. X., Zhang, J., Chen, P. F., Ji, H. S., & Dere, K. 2006, ApJ, 651, 1238